Selective Detection of Acetone and Hydrogen Sulfide for the Diagnosis of Diabetes and Halitosis Using SnO$_2$ Nanofibers Functionalized with Reduced Graphene Oxide Nanosheets

Seon-Jin Choi,[†] Bong-Hoon Jang,[†] Seo-Jin Lee,[†] Byoung Koun Min,[‡] Avner Rothschild,[§] and Il-Doo Kim*,[†]

[†]Department of Materials Science and Engineering, Korea Advanced Institute of Science and Technology, 291 Daehak-ro, Yuseong-gu, Daejeon 305-701, Republic of Korea

[‡]Clean Energy Research Center, Korea Institute of Science and Technology, Seoul 136-791, Republic of Korea

[§]Department of Materials Science and Engineering, Technion - Israel Institute of Technology, Haifa 32000, Israel

Ⓢ Supporting Information

ABSTRACT: Sensitive detection of acetone and hydrogen sulfide levels in exhaled human breath, serving as breath markers for some diseases such as diabetes and halitosis, may offer useful information for early diagnosis of these diseases. Exhaled breath analyzers using semiconductor metal oxide (SMO) gas sensors have attracted much attention because they offer low cost fabrication, miniaturization, and integration into portable devices for noninvasive medical diagnosis. However, SMO gas sensors often display cross sensitivity to interfering species. Therefore, selective real-time detection of specific disease markers is a major challenge that must be overcome to ensure reliable breath analysis. In this work, we report on highly sensitive and selective acetone and hydrogen sulfide detection achieved by sensitizing electrospun SnO$_2$ nanofibers with reduced graphene oxide (RGO) nanosheets. SnO$_2$ nanofibers mixed with a small amount (0.01 wt %) of RGO nanosheets exhibited sensitive response to hydrogen sulfide (R_{air}/R_{gas} = 34 at 5 ppm) at 200 °C, whereas sensitive acetone detection (R_{air}/R_{gas} = 10 at 5 ppm) was achieved by increasing the RGO loading to 5 wt % and raising the operation temperature to 350 °C. The detection limit of these sensors is predicted to be as low as 1 ppm for hydrogen sulfide and 100 ppb for acetone, respectively. These concentrations are much lower than in the exhaled breath of healthy people. This demonstrates that optimization of the RGO loading and the operation temperature of RGO−SnO$_2$ nanocomposite gas sensors enables highly sensitive and selective detection of breath markers for the diagnosis of diabetes and halitosis.

KEYWORDS: reduced graphene oxide, electrospinning, SnO$_2$ nanofibers, exhaled breath analysis, gas sensors
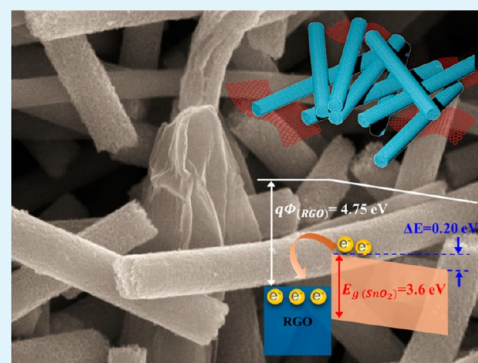
INTRODUCTION

Exhaled breath analysis offers noninvasive and simple diagnosis of various diseases by examining the concentrations of some volatile organic compounds (VOCs) that are known as breath markers for the respective diseases. Significant advances have been reported for the diagnosis of diabetes (acetone),[1,2] lung cancer (toluene),[3] types of heart disease (e.g., myocardial infarction) (pentane),[4] chronic obstructive pulmonary disease (COPD) (carbon monoxide),[5] and kidney disorder (ammonia)[6] by breath analysis methods. In most cases, gas chromatography−mass spectrometry (GC-MS) is used for the precise detection of traces of breath markers.[3,4,7] However, GC-MS has critical limitations for portable use and real-time diagnosis owing to the bulky size and complicated analysis process. Recently, exhaled breath analyzers using semiconductor metal oxide (SMO) gas sensors have been proposed as potential candidates for the diagnosis of various diseases. These analyzers offer important advantages with respect to GC-

MS systems, such as easy miniaturization for portable use, low cost, and simple diagnosis using advanced pattern recognition techniques.[1,2,8−10] For accurate breath analysis and early detection of diseases, the gas sensors must be sensitive enough to detect ppb (part per billion) traces of VOCs in the exhaled breath. This can be achieved, potentially, using 1D nanostructures with large surface-to-volume ratio and high open porosity, which are known for their high gas sensitivity.[11] For example, SnO$_2$ nanofibers,[12] CuO nanowires,[13] In$_2$O$_3$ nanowires,[14] α-Fe$_2$O$_3$ nanochains,[15] and hierarchical In$_2$O$_3$ nanospheres and nanocubes[16] have been proposed for the detection of sub-ppm traces of NO$_2$, hydrogen sulfide (H$_2$S), CO, H$_2$, and ethanol, respectively.
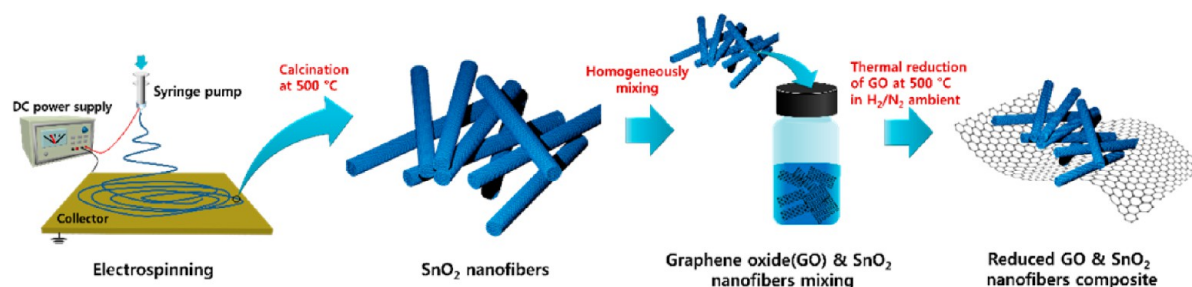
Figure 1. Schematic illustration of the fabrication process of RGO NS−SnO$_2$ NF composite sensing layers. SnO$_2$ NFs were prepared by electrospining of Sn precursor in solution with PVP and PMMA followed by calcination at 500 °C. Subsequently, the SnO$_2$ NFs were mixed in solution with graphene oxide (GO) NSs. Finally, the GO−SnO$_2$ composite material was thermally reduced by annealing in forming gas to form reduced graphene oxide (RGO) NSs mixed with SnO$_2$ NFs.

Among the various fabrication methods for producing highly sensitive 1D nanostructures, electrospinning is one of the most facile routes to produce metal oxide nanofibers (NFs) with high surface-to-volume ratio and exceptional sensitivity to gases.[17] There are several reports on SMO gas sensors produced by electrospinning suggesting their potential use for exhaled breath analysis. They include WO$_3$ NFs[2,8] and SnO$_2$ NFs[10] proposed for the diagnosis of diabetes and halitosis. More recently, SMO−graphene nanocomposite structures such as reduced graphene oxide (RGO)-sensitized Cu$_2$O nanowires,[18] graphene−SnO$_2$,[19] RGO−SnO$_2$,[20] and graphene−Cu$_2$O[21] were proposed for enhanced sensitivity toward NO$_2$, NH$_3$, H$_2$, and H$_2$S gases, respectively. However, the gas sensing tests in these reports were carried out mostly in dry atmosphere, whereas the exhaled breath is very humid and the humidity may influence the sensitivity to the target analytes.[22,23] Nonetheless, these studies demonstrated enhanced gas responses obtained by sensitization of the SMO with graphene or RGO. The sensitization effect was attributed to increased surface area due to the large specific surface area of the graphene nanosheets (NSs) and to enhanced electron transport in graphene−SMO nanocomposite structures. However, detailed understanding of the role of graphene or RGO in the sensing mechanism of nanocomposite gas sensors remains lacking.

Besides high sensitivity, selectivity is another key challenge for the accurate diagnosis of various diseases using exhaled breath analyzers. Given the high humidity (85−95% RH) in exhaled breath, one of the most deleterious interfering species is water vapor which is known to influence the sensitivity of SMO gas sensors.[22,24] Several routes have been proposed to address the challenge of selective detection of specific disease markers in exhaled breath. They include functionalization by noble metal catalysts or promoters,[25] modulation of the operation temperature,[26] use of specific surface additives such as sulfanilic acid or hygroscopic salts,[25] and use of molecular sieve filters.[25]

In this work we report on highly sensitive and selective detection of H$_2$S and acetone in humid air, achieved by mixing RGO NSs with SnO$_2$ NFs (Figure 1). 1D nonwoven mats of SnO$_2$ NFs with high surface-to-volume ratio were produced by electrospinning followed by high temperature calcination. Subsequently, the SnO$_2$ NFs were mixed with graphene oxide (GO) NSs, and in the last step the GO NSs were reduced to RGO NSs by annealing in forming gas (H$_2$/N$_2$ mixture). The loading content of RGO NSs in the RGO−SnO$_2$ nanocomposite sensing layers was tuned to tailor different sensing properties with enhanced sensitivity and selectivity toward H$_2$S or acetone. On top of that, we also tuned the operation

temperature of the sensor to further enhance the selectivity to these gases. The sensitization effect of the RGO NSs was investigated, as described in the following.

EXPERIMENTAL SECTION

Preparation of SnO$_2$ NF. All chemicals used in the electrospinning process to fabricate SnO$_2$ NFs were purchased from Aldrich and used as received without further purification. Highly crystallized SnO$_2$ NFs were achieved by electrospinning and a subsequent calcination step in air ambient. A total of 0.2 g of polyvinylpyrrolidone (PVP, M_w = 1 300 000 g/mol) and 0.2 g of polymethylmethacrylate (PMMA, M_w = 350 000 g/mol) were dissolved in 2.831 g of N,N-dimethylformamide (DMF) solution at room temperature. Subsequently, 0.4 g of tin(IV) acetate and 0.11 g of acetic acid were added to the polymer solution. The solution was homogeneously mixed by stirring at 500 rpm with a magnetic bar for 48 h. Subsequently, the solution was poured into the plastic syringe to which a 21 gauge stainless steel needle was attached. A high voltage (15 kV, DC) was applied between the needle and the collector plate, placed at a distance of 15 cm below the needle. The electrospun polymer/tin precursor layers were annealed in an electrical furnace (Vulcan 3-550, Ney). Polycrystalline SnO$_2$ NFs were obtained following heat treatment at 500 °C for 1 h in air atmosphere.

Material Characterization. The morphology of the RGO-loaded SnO$_2$ nanocomposite layers was examined using scanning electron microscopy (SEM, XL-30 SFEG, Philips). The crystal structure of pristine SnO$_2$, pristine GO, GO-loaded SnO$_2$, and RGO-loaded SnO$_2$ nanocomposite layers was analyzed with X-ray diffraction (XRD, D/MAX-RC 12 kW, Rigaku) using Cu Kα radiation (λ = 1.54 Å). The microstructure of pristine SnO$_2$ NFs and RGO−SnO$_2$ nanocomposite layers was examined by field-emission transmission electron microscopy (FETEM, Tecnai G^2 F30 S-Twin, FEI). Raman spectroscopy analysis was performed on GO-loaded SnO$_2$ nanocomposite layer before and after the thermal reduction process. The chemical composition and bonding state of the main elements were investigated by X-ray photoelectron spectroscopy (XPS, Sigma Probe, Thermo VG Scientific) with Al Kα radiation (1486.6 eV). The work function of pristine RGO NSs and pristine SnO$_2$ NFs were measured by ultraviolet photoelectron spectroscopy (UPS, Sigma Probe, Thermo VG Scientific).

Fabrication of RGO NS-Loaded SnO$_2$ Nanocomposite Layers. The SnO$_2$ NFs were mixed with GO NSs as follows: First, the electrospun and calacined SnO$_2$ NFs were dispersed in ethanol solution. Then, GO NSs were attained by exfoliation of graphite by Hummers and Offeman's method[27] and dispersed in DI water. Subsequently the GO/water suspension was mixed with the SnO$_2$ NF/ethanol dispersed solution. The GO content in the mixed solution was controlled to have 0.01 or 5 wt % of GO relative to the amount of SnO$_2$ NFs dispersed in the mixed solution. The mixed solution was sonicated for 5 min to homogenize the solution. Subsequently the solution was drop-coated on Al$_2$O$_3$ sensor substrates with two parallel Au electrodes on the front side and a microheater on the back side.
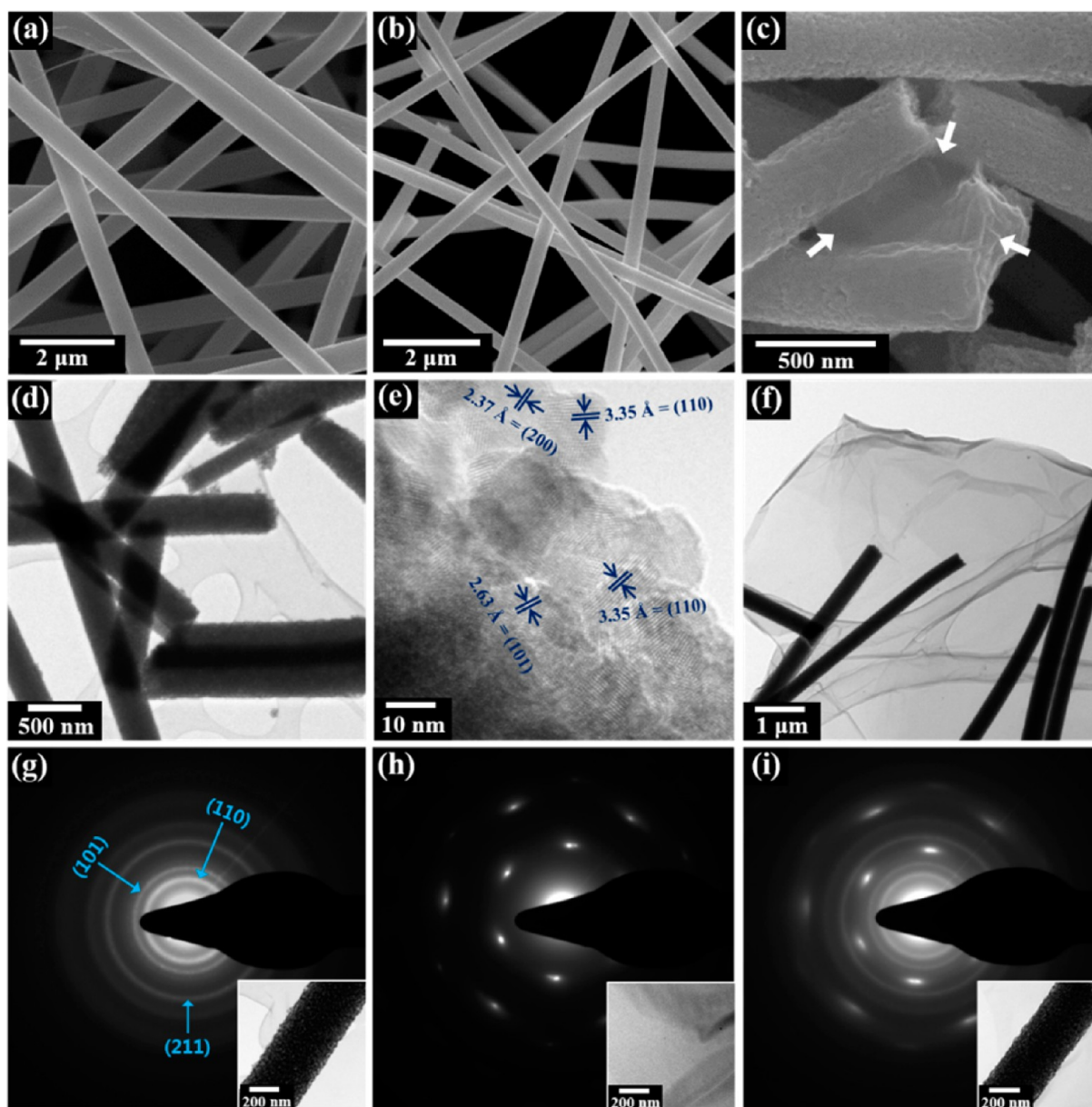
Figure 2. SEM micrographs of Sn precursor/polymer composite NFs in the as-spun state (a) and after calcination (b) and of RGO NS (white arrows)−SnO_2 NF composite layer (c). TEM (d) and HRTEM microspheres (e) of the pristine SnO_2 NFs, and TEM image of RGO NS-SnO_2 NF composite layer (f). SAED patterns of pristine SnO_2 NFs (g), isolated RGO NSs (h), and RGO NS-SnO_2 NF nanocomposite structure (i).

Finally, the GO NS-loaded SnO_2 NFs coated sensors were thermally reduced by annealing in forming gas (20% H_2 in N_2) at 500 °C for 1 h.

Gas Sensor Testing. The gas sensor characteristics of all the sensors were measured in a specialized gas sensor testing system that was described elsewhere.[2] The sensors were stabilized for ∼6 h in the baseline gas (humid air) at the operating temperature prior to the gas sensing tests. Considering the breath sensor application, the humidity level in the baseline air was maintained in the range of 85−95% RH. Traces of H_2S and acetone analytes were used as breath markers for halitosis and diabetes, respectively, based on previous clinical work described in the Introduction. The concentration of these analytes was tuned between 1 and 5 ppm, mixed in the baseline air, by controlling the flow rates of the test gas and baseline air while keeping a constant flow rate of 1000 sccm. Cyclic exposures of 10 min to the test gas followed by 10 min in the baseline air were performed. The resistance of the sensor was measured using a data acquisition system (34972A, Agilent) with a 16 channel multiplexer (34902A, Agilent). The measured resistance was converted into the R_{air}/R_{gas} ratio (where R_{air} is the sensor resistance in the baseline air and R_{gas} is the resistance

measured during exposure to the test gas) that is defined here as the response signal. The temperature control was accomplished by applying voltage to the microheater using a DC power supply (E3647A, Agilent) following a temperature calibration curve that had been measured using a thermocouple attached to the surface of the sensor.

■ RESULTS AND DISCUSSION

Figure 2 shows the microstructural evolution of SnO_2 NFs from the as-spun state to the calcined state (Figure 2a,b, respectively), and the microstructure of SnO_2 NFs mixed with RGO NSs is the final calcined step (Figure 2c). The SEM micrographs reveal that the pristine SnO_2 NFs (without RGO) assembled in nonwoven mats and that the surface of the NFs was smooth in the as-spun state (Figure 2a). The average diameter of the as-spun Sn precursor/polyvinylpyrollidone (PVP) and polymethylmethacrylate (PMMA) NFs was 555 ±

70 nm, and their length was over several tens of micrometers (Figure 2a). After calcination at 500 °C for 1 h, the fiber diameter shrunk to 370 ± 65 nm and their morphology displayed aggregated nanosized SnO_2 grains (Figure 2b). The SnO_2 NFs were functionalized with RGO NSs by mixing SnO_2 NFs dispersed in ethanol and graphene oxide (GO) NSs dispersed in DI water, followed by thermal reduction of the GO NS to RGO NSs by annealing at 500 °C for 1 h in forming gas (H_2/N_2 gas mixture with 20% H_2). This resulted in SnO_2 NFs that were attached to both sides of the large area RGO NSs (marked by the white arrows in Figure 2c). TEM examination revealed that the calcined SnO_2 NFs had multiple contacts at the interface between individual SnO_2 NFs (Figure 2d). High resolution TEM analysis of the calcined SnO_2 NFs displayed lattice fringes corresponding to the Cassiterite structure with interplanar distances of 3.35, 2.63, and 2.37 Å that correspond to the (110), (101), and (200) crystallographic planes, respectively (Figure 2e). The TEM micrograph of the RGO NS−SnO_2 NFs composite structure shows several SnO_2 NFs that were immobilized on folded RGO NSs (Figure 2f). In addition, well-distributed RGO NSs between SnO_2 NFs were confirmed by SEM and EDX elemental mapping of the carbon component with different RGO concentrations (Figure S1 in the Supporting Information). These observations, as it will turn out in the following, are important for the understanding of the electrical transport properties and the sensing mechanism of the RGO−SnO_2 nanocomposite layers. The selected area electron diffraction (SAED) pattern in Figure 2g reveals the polycrystalline structure of the pristine SnO_2 NFs. The SAED pattern of isolated RGO NSs (without SnO_2 NFs) display graphitic crystalline structure, i.e., hexagonal structure with the AB stacking order (Figure 2h).[28] The composite structure of RGO NSs mixed with SnO_2 NFs display a mixed SAED pattern of the RGO NSs and the SnO_2 NFs (Figure 2i).

X-ray diffraction (XRD) analysis was performed to examine the crystal structures of pristine SnO_2 NFs, pristine GO NSs, GO-loaded SnO_2 NFs, and RGO-loaded SnO_2 NFs nano-composites (Figure S2 in the Supporting Information). The pristine GO NSs exhibited a broad peak at $2\theta = 9.64°$ which corresponds to an interplanar distance of 9.15 Å, in agreement with previous work on graphene oxide.[29] The X-ray diffractrogram of the pristine SnO_2 NFs displayed peaks at Bragg angles (2θ) of 26.6°, 33.7°, 38.1°, 51.9°, and 54.4°, which correspond to the (110), (101), (200), (211), and (220) Bragg peaks of the Cassiterite SnO_2 structure (JCPDS file no. 77-0447). This observation is consistent with the lattice fringes in the HRTEM micrograph (Figure 2e) and the SEAD pattern (Figure 2g) of the pristine SnO_2 NFs. The X-ray diffractograms of GO-loaded SnO_2 NFs and RGO-loaded SnO_2 NFs displayed characteristic Bragg peaks of the SnO_2 Cassiterite structure, but the characteristic Bragg peak of GO at $2\theta = 9.64°$ was not observed, most likely due to the low content of GO in this specimen that was below the detection limit of the diffractometer.

To confirm the existence of GO and the reduced state of GO (i.e., RGO) in our specimens, we carried out Raman spectroscopy measurements of pristine SnO_2 NFs, GO-loaded SnO_2, and RGO−SnO_2 composites after the thermal reduction process (Figure 3). The Raman spectroscopy measurements were carried out with an excitation laser source of 514 nm. The pristine SnO_2 NFs showed a sharp Raman peak at a wavelength of 621 cm^{-1} (Figure 3a), which corresponds to the character-istic peak of the SnO_2 Cassiterite structure.[30] The Raman
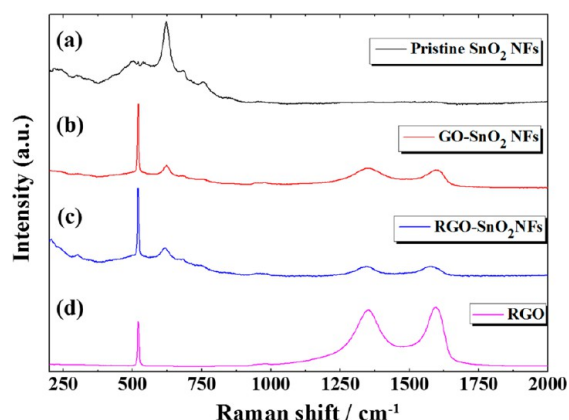

Figure 3. Raman spectra (for 514 nm excitation) of pristine SnO_2 NFs (a), GO-SnO_2 NF composite (b), RGO-SnO_2 NF composite after thermal reduction in forming gas (c), and pristine RGO (d).

spectrum of the GO-loaded SnO_2 NFs showed another peaks besides the SnO_2 peak at 621 cm^{-1} (Figure 3b). The G band peak at 1595 cm^{-1} corresponds to the first-order scattering of the E_{2g} mode of sp^2 domains in the graphene NSs,[31] and the D band peak at 1352 cm^{-1} indicates defect formation in the graphene NSs due to oxidation.[32] The D/G intensity ratio (I_D/I_G) of GO-loaded SnO_2 NFs was estimated to be 1.06. In the case of the RGO−SnO_2 nanocomposite layer, the characteristic Raman peaks of RGO were shifted to 1343 cm^{-1} (D band) and 1586 cm^{-1} (G band) after the thermal reduction step (Figure 3c).[33] In addition, the D/G intensity ratio increased from 1.06 prior to the reduction step to 1.11 following the reduction step, indicating partial presence of the graphene structure with decreased average size of sp^2 domains following the thermal reduction.[34] For the pristine RGO NSs, the D/G intensity ratio was maintained with the value of 1.05 which is similar to GO prior to the reduction process (Figure 3d). Several studies revealed that the D/G intensity ratio increases slightly or remains the same after the thermal reduction process of GO.[34,35]

The chemical composition and bonding state of the RGO−SnO_2 composite layers as well as pristine SnO_2 NFs were examined by X-ray photoelectron spectroscopy (XPS) (Figure 4 and Figure S3 in the Supporting Information). Figure 4a shows the survey scan XPS spectrum of the RGO−SnO_2 composite layers. The XPS spectrum confirms the presence of three elements—Sn, O, and C—from the SnO_2 NFs and RGO NSs. The high resolution XPS spectrum at in the vicinity of the Sn 3d peak (Figure 4b) shows two distinct peaks at binding energies of 495 and 486.5 eV that correspond to the $3d_{3/2}$ and $3d_{5/2}$ states of Sn^{4+}.[36] The asymmetric O 1s spectrum (Figure 4c) can be resolved into several peaks that correspond to O^{2-}, O^{-}, and O_2^{-} with binding energies of 530.2, 531.0, and 532.2 eV, respectively. These binding energies are characteristic of ionized oxygen species at the SnO_2 surface.[37] Additional peaks at 533 and 529.6−529 eV (Figure 4c) represent C—OH groups and C=O and O=C—OH groups belonging to the RGO.[38] The C 1s high resolution spectrum (Figure 4d) has a main peak in the range of 284.5−285 eV that corresponds to C=C and C—H bonding and three minor peaks at 288.9, 287.7, and 286.2 eV that correspond to O=C—OH, C=O, and C—OH groups, respectively.[38]

In order to examine and compare pristine SnO_2 NFs and RGO NS-SnO_2 NFs composite gas sensors for exhaled breath
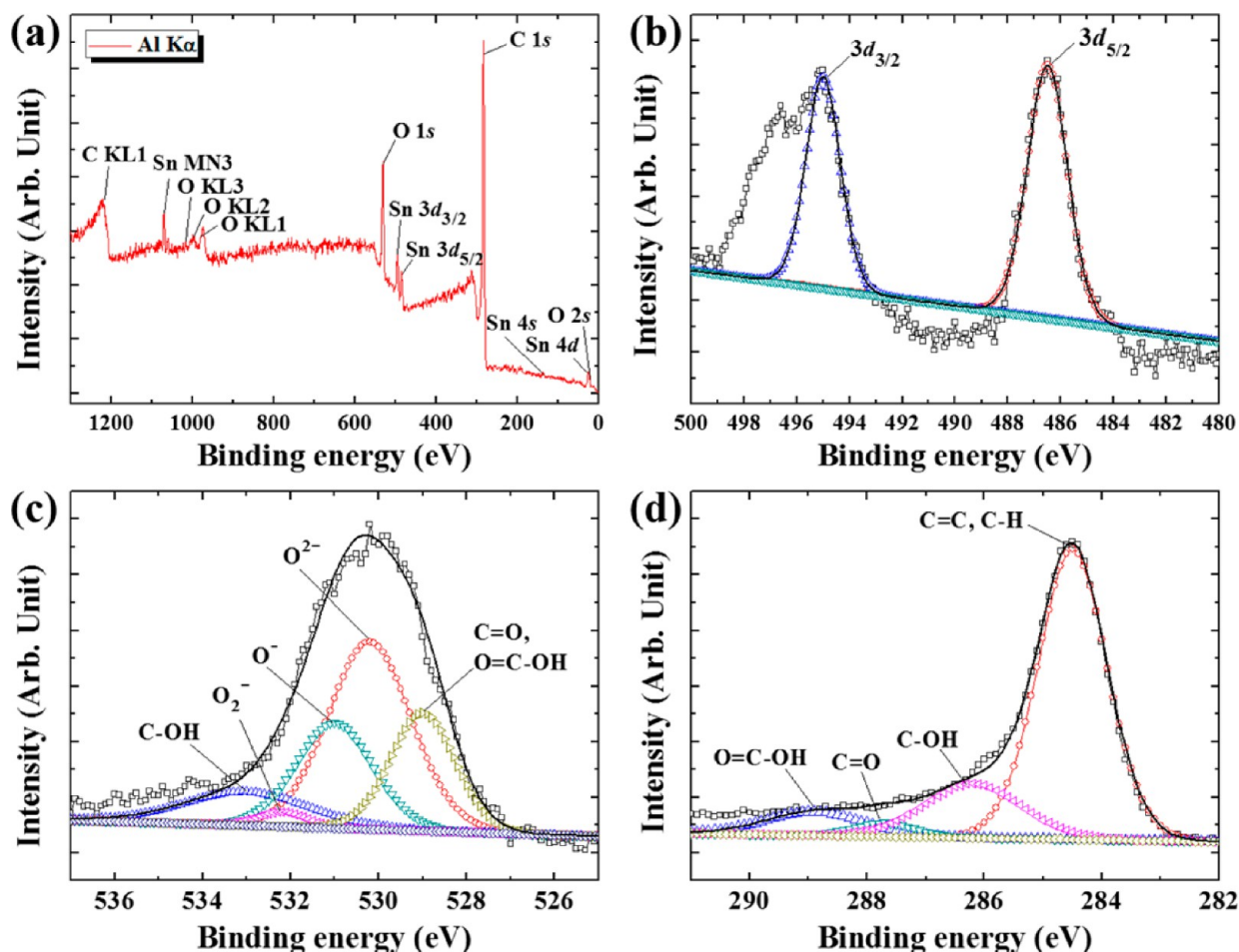
Figure 4. Survey scan XPS spectrum of RGO NS−SnO$_2$ NF composite (a) and high resolution XPS spectra in the vicinity of the Sn 3d (b), O 1s (c), and C 1s peaks (d).

analysis of H$_2$S and acetone for the possible diagnosis of diabetes and halitosis, we carried out gas sensing measurements at residual gas concentrations of these gas analytes in highly humid atmosphere (85−95% RH), comparable to the humidity in the exhaled breath. The gas sensing tests were carried out at different sensor operation temperatures between 150 and 400 °C (Figure 5). On all the tests the response was quick (response time t_{90} < 3.3 min, recovery time < 1.9 min) (Figure S4 in the Supporting Information) and fully reversible, with a stable baseline. The resistance was found to decrease upon exposure to the gas analyte, in both cases (H$_2$S and acetone) and for all the sensors (Figure S6 in the Supporting Information). As shown in Figure 5a, the 0.01 wt % RGO NS-loaded SnO$_2$ NFs displayed the highest response to H$_2$S at 200 °C (R_{air}/R_{gas} = 33.7 at 5 ppm), 7.6 times higher than the response of the pristine SnO$_2$ NFs at the same temperature (R_{air}/R_{gas} = 4.4 at 5 ppm). At high RGO loading of 5 wt % the response to H$_2$S was suppressed (R_{air}/R_{gas} = 1.6 at 5 ppm). In contrast, in the case of acetone sensing the 5 wt % loaded RGO NS-SnO$_2$ nanocomposite sensor displayed the highest response to acetone (R_{air}/R_{gas} = 10.4 at 5 ppm) at an operation temperature of 350 °C (Figure 5b), 2.4 times higher than the response of the pristine SnO$_2$ NFs at the same temperature (R_{air}/R_{gas} = 4.4 at 5 ppm). The response of pristine RGO sensors (Figure S7 in the Supporting Information) was found to be negligible in comparison to the SnO$_2$ NFs and RGO−SnO$_2$ nanocomposite sensors.

To investigate the effect of the operation temperature on the gas sensing properties, the response to 5 ppm of H$_2$S gas or acetone vapor in humid air was measured at different temperatures between 150 and 400 °C (Figure 5c,d for H$_2$S and acetone, respectively). As shown in Figure 5c, the 0.01 wt % RGO NS-loaded SnO$_2$ NFs were most sensitive to H$_2$S at low temperatures, becoming less sensitive to this gas as the temperature increased. The maximal response to 5 ppm H$_2$S was obtained with the 0.01 wt % RGO NS-loaded SnO$_2$ NFs at 200 °C (R_{air}/R_{gas} = 31.6 ± 4.8), dropping down by almost threefold at 350 °C (R_{air}/R_{gas} = 10.6 ± 0.8). The decreased H$_2$S sensing characteristics of the RGO (0.01 wt %)-SnO$_2$ NFs were attributed to the lowering of the optimum operating temperature as well as the increased response when pristine SnO$_2$ NFs were functionalized with RGO (0.01 wt %) via the effective sensitization effect of the RGO, which resulted from an increase in the rate of H$_2$S oxidation. The pristine SnO$_2$ NFs and the 5 wt % RGO NS-loaded SnO$_2$ NFs displayed the opposite trend; their response to H$_2$S increased with increasing temperatures (Figure 5c). The pristine SnO$_2$ NFs showed the lowest response to H$_2$S at 150 °C (R_{air}/R_{gas} = 3.6 ± 0.06), and the response increased to a maximum of 15.0 ± 1.8 at 350 °C. These phenomena were consistent with the findings of previous studies,[39] which demonstrated a shift of the volcano-shaped sensing behavior between the gas response and the temperature toward the lower temperature side as well as an increased volcano top when the metal oxide was sensitized by catalytic
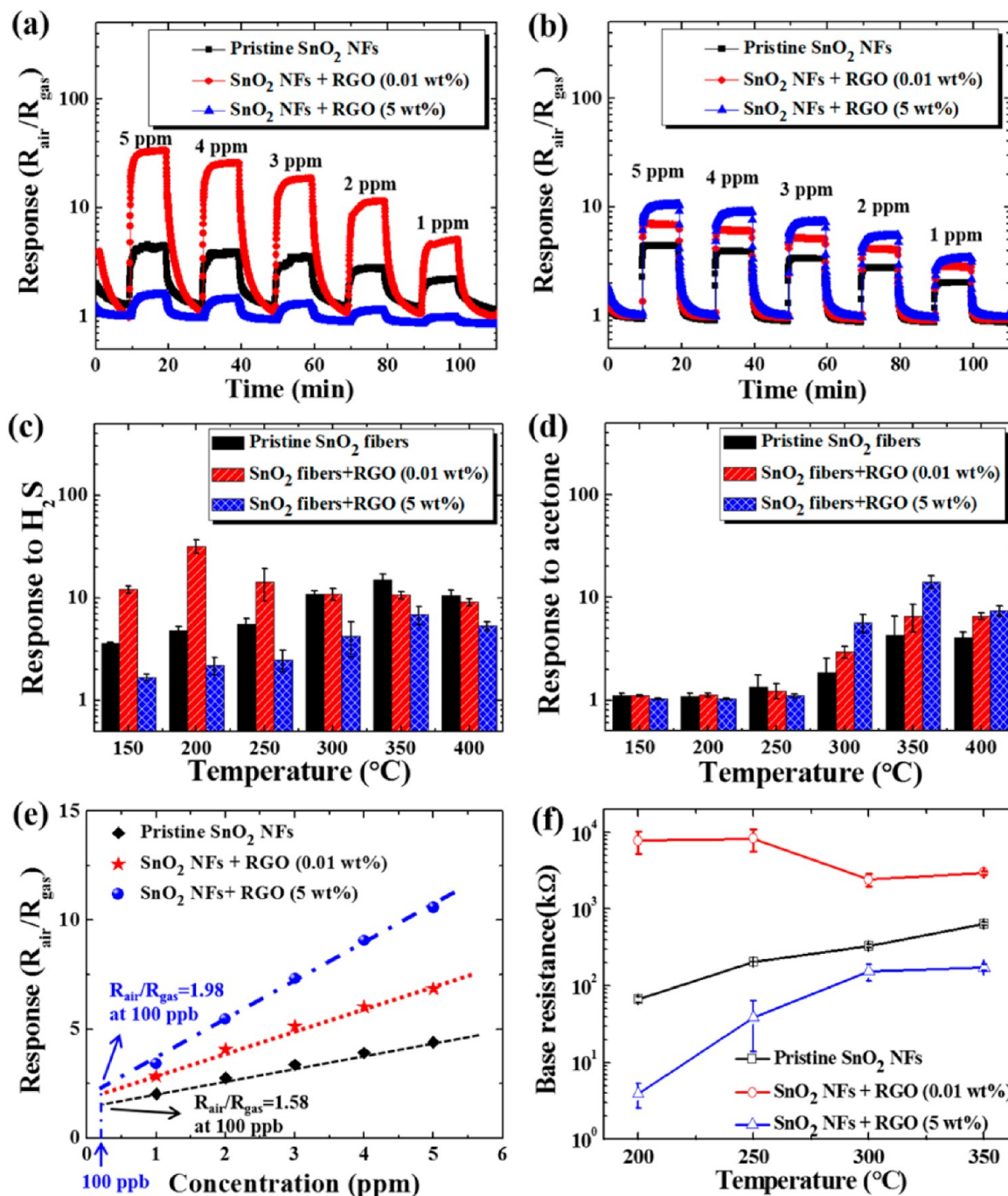
Figure 5. Response of pristine SnO₂ NFs and RGO NS−SnO₂ NF composite sensors upon cyclic exposure to residual H₂S gas concentrations between 1 and 5 ppm in humid air at an operation temperature of 200 °C (a) and upon cyclic exposure to residual acetone concentrations between 1and 5 ppm in humid air at an operation temperature of 350 °C (b). Histogram plots of the steady-state response (R_{air}/R_{gas}) to 5 ppm of H₂S (c) or acetone (d) in humid air at temperatures between 150 and 400 °C. Extrapolated results from part (b) to evaluate the detection limit to acetone (e). The baseline resistivity of the sensors in humid air as a function of temperature (f).

materials such as Pt, Pd, and Au. The 5 wt % RGO NS-loaded SnO₂ NFs had the lowest sensitivity to H₂S among these sensors, and the response increased with increasing temperatures up to a value of 6.8 ± 1.4 at 350 °C.

In case of the acetone sensing characteristics, the response of all three sensors increased with increasing temperatures up to 350 °C (Figure 5d). The most sensitive sensor was the 5 wt % RGO NS-loaded SnO₂ sensor, reaching a maximal response (R_{air}/R_{gas} = 14.2 ± 2.0) at 350 °C. The effect of RGO NSs on the acetone sensitivity was negligible at low operation

temperatures (150 to 250 °C), but it became considerable at higher operation temperatures (300 to 400 °C). The response to acetone was enhanced with increasing RGO loading. We investigated the gas responses of pure SnO₂ NFs which were heat-treated in a forming gas atmosphere (500 °C in 20% H₂/N₂ ambient). Negligible response variation between pristine SnO₂ NFs and the reduced SnO₂ NFs was observed toward H₂S and acetone (Figure S5 in the Supporting Information).

The detection limit of acetone was evaluated by linear extrapolation of the response as a function of acetone
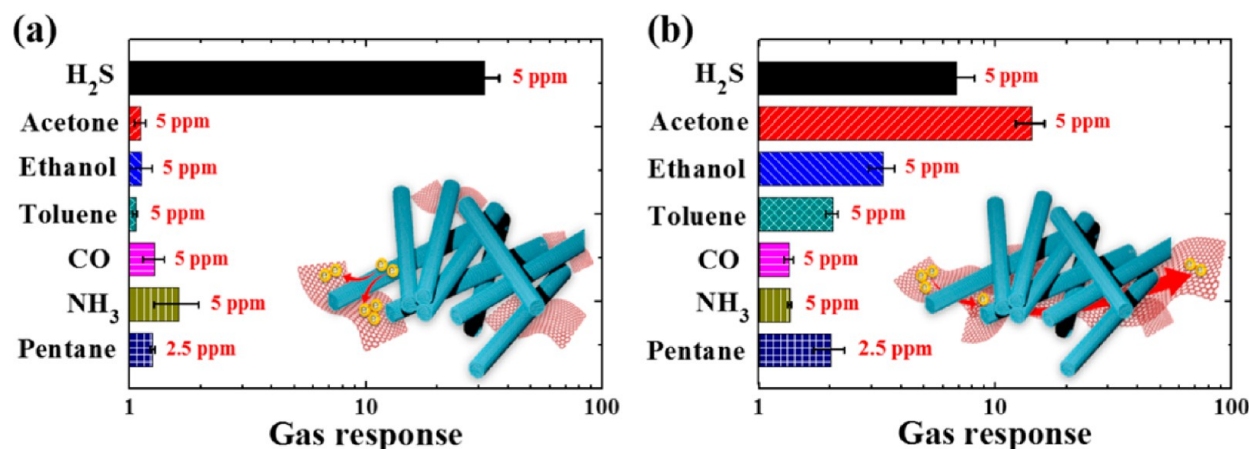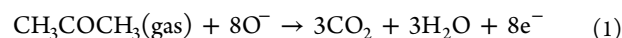
Figure 6. Selective characteristics of (a) RGO NS (0.01 wt %)−SnO$_2$ NFs toward H$_2$S at 200 °C and (b) RGO NS (5 wt %)−SnO$_2$ NF toward acetone at 350 °C with respect to the interfering gases of ethanol, toluene, carbon monoxide, ammonia, and pentane.

concentration (using results from Figure 5b), predicting a response (R_{air}/R_{gas}) of 2.0 on exposure to 100 ppb acetone for the 5 wt % RGO NS-loaded SnO$_2$ sensor, operated at 350 °C (Figure 5e). By extrapolating the response to H$_2$S down to 1 ppm, taking results from Figure 5a, the 0.01 wt % RGO NS-loaded SnO$_2$ sensor is predicted to show a response of 5.1 upon exposure to 1 ppm H$_2$S at 200 °C. This is more than double the predicted response (R_{air}/R_{gas} = 2.2) of the pristine SnO$_2$ NFs at the same acetone concentration (1 ppm) and operation temperature (200 °C). The acetone concentration in the exhaled breath of healthy people is typically in the range of 300 to 900 ppb, whereas for diabetes patients it increases above 1.8 ppm.[1] Our results suggest that the 5 wt % RGO NS-loaded SnO$_2$ NFs sensor can easily detect acetone in humid air at these concentrations. With regard to H$_2$S it was reported that the odor recognizable concentration of H$_2$S in the exhaled breath of halitosis patients is 1 ppm,[40] well within the detectable range of H$_2$S of the 0.01 wt % RGO NS-loaded SnO$_2$ sensor. The low detection limit and superior response of RGO NS-loaded SnO$_2$ NFs demonstrates sensitive detection of acetone and H$_2$S for potential diagnosis of diabetes and halitosis.
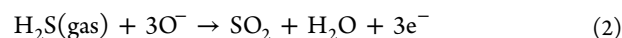
The effect of interfering gases such as ethanol, toluene, carbon monoxide, ammonia, and pentane, which are known as biomarkers for the diagnosis of blood-alcohol concentrations, lung cancer,[3] certain types of heart disease (e.g., myocardial infarction),[4] chronic obstructive pulmonary disease (COPD),[5] and kidney failure,[6] were confirmed with composites of RGO NS−SnO$_2$ NFs (Figure 6). The results revealed that RGO NS (0.01 wt %)−SnO$_2$ NFs exhibit highly H$_2$S-selective sensing characteristics (R_{air}/R_{gas} = 31.6 ± 4.8) with a minor response (<1.6) toward interfering gases at an operating temperature of 200 °C. In addition, high acetone-selective sensing properties were observed with RGO (5 wt %)−SnO$_2$ NFs (R_{air}/R_{gas} = 14.2 ± 2.0) at an operating temperature of 350 °C though these were slightly less selective toward H$_2$S (R_{air}/R_{gas} = 6.8 ± 1.4) and ethanol (R_{air}/R_{gas} = 3.3 ± 0.4) compared to the other interfering gases. To understand the gas sensing characteristics of RGO NS-loaded SnO$_2$ NFs, we begin by considering the sensing mechanism of n-type SMO gas sensors. This involves resistance changes induced by chemisorption of oxygen adions (O$^-$, O^{2-}) that interact with reducing gases, thereby modifying the surface depletion region and the sensor resistance.[25,41] When reducing gases such as H$_2$S or acetone adsorb on the SMO sensor, preadsorbed oxygen adions are released to the

atmosphere in the form of CO$_2$, H$_2$O, and SO$_2$ according to the following chemical reactions:

For acetone:[42]

$$CH_3COCH_3(gas) + 8O^- \rightarrow 3CO_2 + 3H_2O + 8e^- \qquad (1)$$

For H$_2$S:[43]

$$H_2S(gas) + 3O^- \rightarrow SO_2 + H_2O + 3e^- \qquad (2)$$

As a result, electrons that were trapped in the oxygen adions return back to the conduction band of the n-type SMO, thereby the resistance decreases upon exposure to these gases. The experimental results of the pristine SnO$_2$ NF sensors are consistent with this mechanism, displaying a decrease in the resistance upon exposure to H$_2$S or acetone in humid air (Figure S6a, b in the Supporting Information). This is the typical behavior of n-type SMO gas sensors upon exposure to reducing gases. Stepping from the pristine SnO$_2$ NFs to the RGO NS−SnO$_2$ nanocomposite sensors, we have to consider first the effect of RGO NSs on the electrical transport properties of the nanocomposite structure. Toward this end, we examine the baseline resistance of the RGO NS-loaded SnO$_2$ sensors in comparison to that of the pristine SnO$_2$ sensor (Figure 5f). Mixing the SnO$_2$ NFs with a small amount (0.01 wt %) of RGO NSs increases the resistance by one to two orders of magnitude (depending on the temperature). At such a small RGO concentration there is no percolation path through the RGO NSs so the current flows through the interconnected network of SnO$_2$ NFs. The higher resistance of the 0.01 wt % RGO NS-loaded SnO$_2$ sensor with respect to the pristine SnO$_2$ sensor (Figure 5f) indicates electron transfer from the SnO$_2$ NFs to the RGO NSs and localization in isolated RGO NSs. This observation is consistent with a previous report on electron transfer from TiO$_2$ nanoparticles to RGO NSs.[44] In the case of the 0.01 wt % RGO NS-loaded SnO$_2$ sensor, the electrons transferred from the SnO$_2$ NFs to the RGO NSs are localized (trapped) in the isolated RGO NSs and therefore they do not contribute to the current flow through the sensor. Therefore, the resistance of the 0.01 wt % RGO NS-loaded SnO$_2$ sensor is much higher than that of the pristine SnO$_2$ sensor. The increased base resistance of SnO$_2$ NFs at the increased operating temperatures can be interpreted as stemming from the generation of thermally exited electrons considering that the oxygen adsorption on the SnO$_2$ surface is mainly controlled by the electron supply.[45] For the RGO NS (5
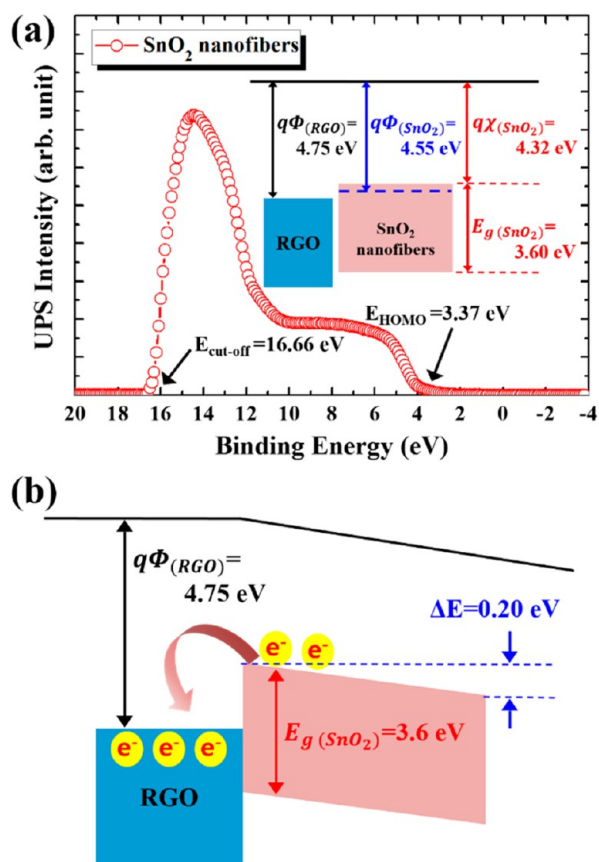
Figure 7. (a) Ultraviolet photoelectron spectroscopy (UPS) spectrum of SnO_2 NFs and the schematic energy band structure of RGO NSs and SnO_2 NFs before forming the electrical junction state in the inset and (b) schematic illustration of band bending of RGO NS–SnO_2 NF after making the junction structure.

wt %)–SnO_2 NF sensor, the current flow of which depends on the continuous percolation path of the RGO, more electrons can be trapped in the RGO NSs at higher temperatures due to the thermally excited electrons, resulting in an increase in the base resistance due to the reduced hole concentration.

To confirm that RGO NSs are indeed acceptors for electrons from the SnO_2 NFs we carried out ultraviolet photoelectron spectroscopy (UPS) analysis of the energy band alignment between the RGO NSs and SnO_2 NFs (Figure 7). The UPS spectrum of pristine SnO_2 NFs has a cutoff energy (E_{cutoff}) of 16.66 eV and a HOMO energy (E_{HOMO}) of 3.37 eV (Figure 7a), indicating that the work function and electron affinity of the SnO_2 NFs are 4.55 and 4.32 eV, respectively. The UPS spectrum of pristine RGO NSs (not shown) revealed that the work function of the RGO NSs was 4.75 eV. Thus, when RGO NSs are in contact with SnO_2 NFs, electrons transfer from the low work function SnO_2 NFs to the high work function RGO NSs, and a Schottky barrier of 0.2 eV is formed at the RGO/SnO_2 junction (Figure 7b). This explains the high resistance of the 0.01 wt % RGO NS-loaded SnO_2 sensor (Figure 5f).

The 5 wt % RGO NS-loaded SnO_2 sensor is quite different than the pristine SnO_2 NFs and 0.01 wt % RGO NS-loaded SnO_2 sensors because at such a high loading level the RGO NSs form continuous percolation pathways through the sensor. Due to the higher conductivity of RGO NSs in comparison to that of SnO_2, the resistance of the 5 wt % RGO NS-loaded SnO_2 sensor is smaller than that of the pristine SnO_2 sensor (Figure

5f). Unlike the pristine SnO_2 NFs and 0.01 wt % RGO NS-loaded SnO_2 sensors that conduct electrical current through the SnO_2 NFs network, the conductivity of the 5 wt % RGO NS-loaded SnO_2 sensor is dominated by the RGO NSs that conduct most of the current.

Armed with this knowledge we can now explain the sensitivity trends observed in Figure 5. Adding a small amount (0.01 wt %) of RGO NSs to the SnO_2 NFs enhances their sensitivity to H_2S because it reduces the free carrier (electron) concentration in the SnO_2 NFs (by trapping electrons in isolated RGO NSs), thereby the sensitivity to gas-modulated surface conductivity changes is enhanced.[46] In this case the RGO NSs sensitize the response of the SnO_2 NFs to reducing gases in a similar way to the sensitization effect of p-type nanoparticles such as NiO, CuO, and PdO attached to SnO_2 NFs.[12,47] In other words, the trapped electrons which attracted chemisorbed oxygen species on the surfaces of the RGO NSs can be released by exposure to H_2S, resulting in enhanced surface conductivity changes of the SnO_2 NFs. However, adding a large amount (5 wt %) of RGO NSs to the SnO_2 NFs completely changes the situation, inverting the dominant transport mechanism and sensor characteristics from those of the SnO_2 NFs to those of the RGO NSs. This is because at 5 wt % loading the RGO NSs form continuous percolation pathways through the sensor that, given the high conductivity of RGO NSs compared to that of SnO_2 NFs, dominate the electrical transport and gas sensing properties of the nanocomposite sensor. Therefore, in this case it is the SnO_2 NFs that sensitize the response of the RGO NSs to oxidizing analytes by donating electrons that can be stored in the RGO NSs and shuttled to electron acceptor species[46] such as acetone molecules.[48] It should be noted that decreased resistance was observed in pristine p-type RGO upon exposure to an electron-acceptor species, acetone in this case, thereby increasing the hole carrier concentration.[48] The p-type character of RGO NSs,[49] energy band alignment between the SnO_2 NFs and RGO NSs (Figure 7b), and the electron acceptor functionalization of acetone on RGO[48] suggest that electrons that were transferred from the SnO_2 NFs and stored in the RGO NSs are withdrawn upon exposure to acetone, thereby restoring the hole concentration and p-type conductivity of the RGO NSs. The sensitization effect of the RGO NSs by SnO_2 NFs is consistent with our own observations of negligible response pristine RGO sensors (see Figure S7 in the Supporting Information) as well as with other reports on pristine RGO sensors to acetone[48] and other VOCs[50] that display much milder sensitivity in comparison to our 5 wt % RGO NS–SnO_2 sensor.

■ CONCLUSIONS

In summary, highly selective and remarkably sensitive sensors to H_2S and acetone were produced by mixing SnO_2 NFs with RGO NSs. The SnO_2 NFs were produced by electrospinning, a simple and versatile method for the fabrication of NFs of different materials. Subsequently the SnO_2 NFs were mixed with GO NSs at loading levels of 0.01 or 5 wt % GO, and eventually the GO NSs were reduced to RGO by annealing in forming gas. This resulted in porous nanocomposite layers of SnO_2 NFs mixed with RGO NSs. At the small RGO loading level (0.01 wt %) the electrical transport and gas sensing properties of the nanocomposite layer were dominated by the SnO_2 NFs, but at the high loading level (5 wt % RGO) the RGO NSs formed continuous percolation pathways and they became the dominant component controlling the electrical

transport through the nanocomposite layer. This enabled tuning the gas sensing characteristics of the RGO NS−SnO$_2$ nanocomposite sensors in order to achieve enhanced sensitivity and selectivity to traces of H$_2$S or acetone in humid air for sensors with low or high levels of RGO loading, respectively. Besides changing the RGO/SnO$_2$ ratio we also found that tuning the operation temperature of the sensors enabled achieving high selectivity between H$_2$S and acetone.

The 0.01 wt % RGO NS-loaded SnO$_2$ NFs were very sensitive to H$_2$S with a response (R_{air}/R_{gas}) of 33.7 to 5 ppm H$_2$S at 200 °C, whereas the response to acetone was negligible (R_{air}/R_{gas} = 1.1) at this temperature. On the other hand, the 5 wt % RGO NS-loaded SnO$_2$ NFs displayed high sensitivity to acetone with the response of 10.4 to 5 ppm acetone at 350 °C, with minor cross-sensitivity to H$_2$S (R_{air}/R_{gas} = 6.8). The limit of detection of this sensor was evaluated by extrapolation to low analyte concentrations, predicting a significant response (R_{air}/R_{gas} = 2) to 100 ppb acetone at 350 °C. The detection limit of the 0.01 wt % RGO NS-loaded SnO$_2$ sensor to H$_2$S was predicted to reach sub-ppm levels at 200 °C. These results demonstrate the potential of these sensors for exhaled breath analysis for the diagnosis of halitosis and diabetes by selective detection of disease markers such as H$_2$S and acetone.

■ ASSOCIATED CONTENT

Ⓢ Supporting Information

SEM images and EDX elemental mapping to confirm the RGO distributions; XRD analysis; sensing characteristics of reduction-treated SnO$_2$ NFs; and sensor response/recovery times; resistivity changes and gas sensing characteristics of RGO. This material is available free of charge via the Internet at http://pubs.acs.org.

■ AUTHOR INFORMATION

Corresponding Author
*E-mail: idkim@kaist.ac.kr (I.-D.K.).

Notes
The authors declare no competing financial interest.

■ ACKNOWLEDGMENTS

■ REFERENCES

(1) Righettoni, M.; Tricoli, A.; Pratsinis, S. E. *Anal. Chem.* **2010**, *82*, 3581−3587.

(2) Choi, S. J.; Lee, I.; Jang, B. H.; Youn, D. Y.; Ryu, W. H.; Park, C. O.; Kim, I. D. *Anal. Chem.* **2013**, *85*, 1792−1796.

(3) Peng, G.; Tisch, U.; Adams, O.; Hakim, M.; Shehada, N.; Broza, Y. Y.; Billan, S.; Abdah-Bortnyak, R.; Kuten, A.; Haick, H. *Nat. Nanotechnol.* **2009**, *4*, 669−673.

(4) Weitz, Z. W.; Birnbaum, A. J.; Sobotka, P. A.; Zarling, E. J.; Skosey, J. L. *Lancet* **1991**, *337*, 933−935.

(5) Montuschi, P.; Kharitonov, S. A.; Barnes, P. J. *Chest* **2001**, *120*, 496−501.

(6) (a) Narasimhan, L. R.; Goodman, W.; Patel, C. K. N. *Proc. Natl. Acad. Sci. U.S.A.* **2001**, *98*, 4617−4621. (b) Fleischer, M.; Simon, E.; Rumpel, E.; Ulmer, H.; Harbeck, M.; Wandel, M.; Fietzek, C.; Weimar, U.; Meixner, H. *Sens. Actuators, B* **2002**, *83*, 245−249.

(7) (a) Machado, R. F.; Laskowski, D.; Deffenderfer, O.; Burch, T.; Zheng, S.; Mazzone, P. J.; Mekhail, T.; Jennings, C.; Stoller, J. K.; Pyle, J.; Duncan, J.; Dweik, R. A.; Erzurum, S. C. *Am. J. Respir. Crit. Care Med.* **2005**, *171*, 1286−91. (b) Olopade, C. O.; Zakkar, M.; Swedler, W. I.; Rubinstein, I. *Chest* **1997**, *111*, 862−5. (c) Lemoyne, M.; Vangossum, A.; Kurian, R.; Jeejeebhoy, K. N. *Am. J. Clin. Nutr.* **1988**, *48*, 1310−1315.

(8) Shin, J.; Choi, S. J.; Youn, D. Y.; Kim, I. D. *J. Electroceram.* **2012**, *29*, 106−116.

(9) Righettoni, M.; Tricoli, A.; Pratsinis, S. E. *Chem. Mater.* **2010**, *22*, 3152−3157.

(10) Shin, J.; Choi, S. J.; Lee, I.; Youn, D. Y.; Park, C. O.; Lee, J. H.; Tuller, H. L.; Kim, I. D. *Adv. Funct. Mater.* **2013**, *23*, 2357−2367.

(11) Comini, E. *Anal. Chim. Acta* **2006**, *568*, 28−40.

(12) Yang, D. J.; Kamienchick, I.; Youn, D. Y.; Rothschild, A.; Kim, I. D. *Adv. Funct. Mater.* **2010**, *20*, 4258−4264.

(13) Li, X.; Wang, Y.; Lei, Y.; Gu, Z. *RSC Adv.* **2012**, *2*, 2302.

(14) Singh, N.; Gupta, R. K.; Lee, P. S. *ACS Appl. Mater. Interfaces* **2011**, *3*, 2246−2252.

(15) Ma, J.; Mei, L.; Chen, Y.; Li, Q.; Wang, T.; Xu, Z.; Duan, X.; Zheng, W. *Nanoscale* **2013**, *5*, 895−898.

(16) Zai, J. T.; Zhu, J.; Qi, R. R.; Qian, X. F. *J. Mater. Chem. A* **2013**, *1*, 735−745.

(17) (a) Kim, I. D.; Rothschild, A. *Polym. Adv. Technol.* **2011**, *22*, 318−325. (b) Kim, I. D.; Rothschild, A.; Tuller, H. L. *Acta Mater.* **2013**, *61*, 974−1000.

(18) Deng, S.; Tjoa, V.; Fan, H. M.; Tan, H. R.; Sayle, D. C.; Olivo, M.; Mhaisalkar, S.; Wei, J.; Sow, C. H. *J. Am. Chem. Soc.* **2012**, *134*, 4905−4917.

(19) Lin, Q.; Li, Y.; Yang, M. *Sens. Actuators, B* **2012**, *173*, 139−147.

(20) Russo, P. A.; Donato, N.; Leonardi, S. G.; Baek, S.; Conte, D. E.; Neri, G.; Pinna, N. *Angew. Chem.* **2012**, *51*, 11053−11057.

(21) Zhou, L.; Shen, F.; Tian, X.; Wang, D.; Zhang, T.; Chen, W. *Nanoscale* **2013**, *5*, 1564−9.

(22) Kim, H. R.; Haensch, A.; Kim, I. D.; Barsan, N.; Weimar, U.; Lee, J. H. *Adv. Funct. Mater.* **2011**, *21*, 4456−4463.

(23) (a) Qiu, Y. F.; Yang, S. H. *Adv. Funct. Mater.* **2007**, *17*, 1345−1352. (b) Ruminski, A. M.; Moore, M. M.; Sailor, M. J. *Adv. Funct. Mater.* **2008**, *18*, 3418−3426.

(24) Devan, R. S.; Patil, R. A.; Lin, J. H.; Ma, Y. R. *Adv. Funct. Mater.* **2012**, *22*, 3326−3370.

(25) Morrison, S. R. *Sens. Actuators* **1987**, *12*, 425−440.

(26) Lee, A. P.; Reedy, B. J. *Sens. Actuators, B* **1999**, *60*, 35−42.

(27) Hummers, W. S., Jr.; Offeman, R. E. *J. Am. Chem. Soc.* **1958**, *80*, 1339.

(28) Jeong, H. K.; Lee, Y. P.; Lahaye, R. J. W. E.; Park, M. H.; An, K. H.; Kim, I. J.; Yang, C. W.; Park, C. Y.; Ruoff, R. S.; Lee, Y. H. *J. Am. Chem. Soc.* **2008**, *130*, 1362−1366.

(29) Moon, I. K.; Lee, J.; Ruoff, R. S.; Lee, H. *Nat. Commun.* **2010**, *1*, 73.

(30) Sun, S. H.; Meng, G. W.; Zhang, G. X.; Gao, T.; Geng, B. Y.; Zhang, L. D.; Zuo, J. *Chem. Phys. Lett.* **2003**, *376*, 103−107.

(31) Pimenta, M. A.; Dresselhaus, G.; Dresselhaus, M. S.; Cancado, L. G.; Jorio, A.; Saito, R. *Phys. Chem. Chem. Phys.* **2007**, *9*, 1276−91.

(32) (a) Khanra, P.; Kuila, T.; Kim, N. H.; Bae, S. H.; Yu, D. S.; Lee, J. H. *Chem. Eng. J.* **2012**, *183*, 526−533. (b) Yuan, W. H.; Li, B. Q.; Li, L. *Appl. Surf. Sci.* **2011**, *257*, 10183−10187.

(33) Chen, W. F.; Yan, L. F. *Nanoscale* **2010**, *2*, 559−563.

(34) Stankovich, S.; Dikin, D. A.; Piner, R. D.; Kohlhaas, K. A.; Kleinhammes, A.; Jia, Y.; Wu, Y.; Nguyen, S. T.; Ruoff, R. S. *Carbon* **2007**, *45*, 1558−1565.

(35) Hontorialucas, C.; Lopezpeinado, A. J.; Lopezgonzalez, J. D. D.; Rojascervantes, M. L.; Martinaranda, R. M. *Carbon* **1995**, *33*, 1585−1592.

(36) An, G. M.; Na, N.; Zhang, X. R.; Miao, Z. J.; Miao, S. D.; Ding, K. L.; Liu, Z. M. *Nanotechnology* **2007**, *18*, 435707.

(37) Kolmakov, A.; Potluri, S.; Barinov, A.; Mentes, T. O.; Gregoratti, L.; Nino, M. A.; Locatelli, A.; Kiskinova, M. *ACS Nano* **2008**, *2*, 1993−2000.

(38) Yang, D.; Velamakanni, A.; Bozoklu, G.; Park, S.; Stoller, M.; Piner, R. D.; Stankovich, S.; Jung, I.; Field, D. A.; Ventrice, C. A.; Ruoff, R. S. *Carbon* **2009**, *47*, 145−152.

(39) (a) Tao, W. H.; Tsai, C. H. *Sens. Actuators, B* **2002**, *81*, 237−247. (b) Yamazoe, N.; Sakai, G.; Shimanoe, K. *Catal. Surv. Asia* **2003**, *7*, 63−75.

(40) Tangerman, A.; Winkel, E. G. *J. Breath Res.* **2010**, *4*, 017003.

(41) (a) Morrison, S. R. *Sens. Actuators* **1982**, *2*, 329−341. (b) Heiland, G. *Sens. Actuators* **1982**, *2*, 343−361.

(42) Qin, L. P.; Xu, J. Q.; Dong, X. W.; Pan, Q. Y.; Cheng, Z. X.; Xiang, Q.; Li, F. *Nanotechnology* **2008**, *19*, 185705.

(43) Vaishampayan, M. V.; Deshmukh, R. G.; Walke, P.; Mulla, I. S. *Mater. Chem. Phys.* **2008**, *109*, 230−234.

(44) Lightcap, I. V.; Kosel, T. H.; Kamat, P. V. *Nano Lett.* **2010**, *10*, 577−583.

(45) Yamazoe, N.; Shimanoe, K. *Sens. Actuators, B* **2008**, *128*, 566−573.

(46) (a) Rothschild, A.; Komem, Y. *J. Electroceram.* **2004**, *13*, 697−701. (b) Rothshild, A.; Tuller, H. L. *J. Electroceram.* **2006**, *17*, 1005−1012.

(47) Hieu, N. V.; Phung, T. H. V.; Nhan, L. T.; Duy, N. V.; Hoa, N. D. *Appl. Phys. Lett.* **2012**, *101*.

(48) Kehayias, C. E.; MacNaughton, S.; Sonkusale, S.; Staii, C. *Nanotechnology* **2013**, *24*, 245502.

(49) Sreeprasad, T. S.; Berry, V. *Small* **2013**, *9*, 341−350.

(50) (a) Dua, V.; Surwade, S. P.; Ammu, S.; Agnihotra, S. R.; Jain, S.; Roberts, K. E.; Park, S.; Ruoff, R. S.; Manohar, S. K. *Angew. Chem., Int. Ed.* **2010**, *49*, 2154−2157. (b) Lipatov, A.; Varezhnikov, A.; Wilson, P.; Sysoev, V.; Kolmakov, A.; Sinitskii, A. *Nanoscale* **2013**, *5*, 5426−5434.